nature communications

Article

https://doi.org/10.1038/s41467-024-54674-4

Promotion of TLR7-MyD88-dependent inflammation and autoimmunity in mice through stem-loop changes in Lnc-Atg16l1

Received: 29 February 2024

Accepted: 18 November 2024

Zongheng Yang [1,5], **Shuchen Ji** [1,5], **Lun Liu** [1], **Shuo Liu** [1], **Bingjing Wang** [1], **Yuanwu Ma** [2] & **Xuetao Cao** [1,3,4] ✉

Uncontrolled TLR signaling can cause inflammatory immunopathology and trigger autoimmune diseases. For example, TLR7 promotes pathogenesis of systemic lupus erythematosus. However, whether RNA structural changes affect nucleic acids-sensing TLRs signaling and impact disease progression is unclear. Here by iCLIP-seq we identify a TLR7-binding long non-coding RNA, Lnc-Atg16l1, and find that it promotes TLR7 and other MyD88-dependent TLRs signaling in various types of immune cells. Depletion of *Lnc-Atg16l1* attenuates development of TLR7-linked autoimmune phenotypes in the mouse SLE model. Mechanistically, we find that Lnc-Atg16l1 binds to TLR7 at bases near U84 and MyD88 at bases around A129. The analysis of Lnc-Atg16l1 in situ structures show that it strengthens the interaction between TIR domain of TLR7 and MyD88 through specific stem-loop structure changes as a molecular scaffold after TLR7 activation to promote TLR7 downstream signaling. Therefore, we discover a mechanism for host RNA regulation of innate signaling and autoimmune disease through its structural changes. These findings provide insights into the pro-inflammatory function of self RNA in a structure-dependent manner and suggest a potential target for TLR-related autoimmune disorders.

Unlimited inflammation may cause host tissue damage and even leads to autoimmune diseases. Toll-like receptors (TLRs), one of crucial class of pattern recognition receptors (PRRs) in the immune system, can initiate the innate immune response by recognizing pathogen-associated molecular patterns[1]. Thus, TLRs and their downstream signaling should be accurately regulated to prevent the imbalance of immune responses and pathogenesis of immunological disorders[2]. However, the molecular mechanisms underlying this complex network remain incompletely understood.

Specially, TLR7 is an important TLR member that recognizes exogenous single-stranded RNA (ssRNA) to activate downstream innate signaling pathways. TLR7 activation induces pro-inflammatory cytokines and type I interferon (IFN-I) production[1,2]. However, overexpression or abnormal activation of TLR7 signaling in vivo are found to be closely related to the pathogenesis and development of many kinds of autoimmune diseases, including systemic lupus erythematosus[3] and rheumatoid arthritis (RA)[4]. Therefore, clarifying the regulation and underlying mechanism of TLR7 signaling in vivo is critical for treating those autoimmune diseases. It is reported that TLR7 can recognize exogenous GU-rich ssRNAs[5–7]. But the potential endogenous RNAs that are capable of regulating TLR signaling especially TLR7 and associated autoimmune diseases remain unclear.

Long noncoding RNAs (lncRNAs), with various sequences, flexible structures and wild distribution, have been shown to play important roles

---

[1]Department of Immunology, Center for Immunotherapy, Peking Union Medical College, Chinese Academy of Medical Sciences, Beijing, China. [2]Institute of Laboratory Animal Science, Chinese Academy of Medical Sciences, Beijing, China. [3]Institute of Immunology, College of Life Sciences, Nankai University, Tianjin, China. [4]National Key Laboratory of Immunity & Inflammation, Institute of Immunology, Navy Medical University, Shanghai, China. [5]These authors contributed equally: Zongheng Yang, Shuchen Ji. ✉e-mail: caoxt@immunol.org

in inflammation in recent years[8–11]. Compared with proteins, lncRNA functions in cellular processes depend more on intrinsic properties, including structure. Previous studies have shown that the structural changes in RNAs have diverse functional outcomes in cells. For example, structural changes in metabolite-induced riboswitches can regulate gene expression[12], structural changes at the 5′ end of the HIV genome impact genome assembly and transcription[13], and RNA structural changes influence aggregation and phase transition of associated proteins[14]. It's known that diverse changes, such as metabolic reprogramming, epigenetic dynamics and post-translational modifications, occur in SLE patients. Therefore, it is possible that these pathological conditions alter the structure of intracellular RNAs and then impact TLR7 signaling and the progression of TLR7-assoiacted autoimmune diseases.

In this study, we use iCLIP-seq and functional analysis to identify a TLR7-binding lncRNA, Lnc-Atg16l1, which can promote TLR7 and other MyD88-dependent TLRs signaling. We demonstrate that Lnc-Atg16l1 could bind to activated TLR7 and enhance the TLR7 signaling pathway and inflammation by promoting the interaction between TLR7 and MyD88. We also demonstrate that stem-loop structural changes in Lnc-Atg16l1 play an important role in promoting TLR7 signaling, which are also confirmed in a mouse SLE model. Together, our findings demonstrate a general mechanism involving how self-RNA structure affect innate sensors-triggering innate response and autoinflammation, and provide a potential strategy for controlling TLR-related autoimmune diseases.

Results

iCLIP-seq analysis of activated TLR7 identifies Lnc-Atg16l1 as a binding partner

To investigate whether lncRNAs are involved in the regulation of TLR7 signaling, we first constructed RAW264.7 cells with stable TLR7 overexpression. We found that overexpression of TLR7 increased the mRNA expression of *Tnf* and *Il6* in RAW264.7 cells (Fig. 1a), and a predominant C-terminal cleaved fragment of TLR7, which was indicative of TLR7 activation, was also detected (Supplementary Fig. 1a). These data suggest that overexpression of TLR7 leads to spontaneous TLR7 activation without exogenous ssRNA stimulation in RAW264.7 cells, indicating that endogenous RNAs could bind to activated TLR7. We then performed individual-nucleotide resolution crosslinking and immunoprecipitation (iCLIP)[15] to enrich activated-TLR7-binding RNAs in these TLR7-overexpressing RAW264.7 cells (Fig. 1b). Meanwhile, we also isolated endosomes from TLR7-overexpressing RAW264.7 after UV-crosslinking and performed RNA sequencing (RNA-seq) to identify endosome-located RNAs. By overlapping these two sequencing datasets (Endosome RNA sequencing FPKM > 1000, iCLIP RNA sequencing data FPKM > 10 and individual TLR7 truncations), we obtained seven candidate TLR7-binding lncRNAs (Fig. 1c, Supplementary Fig. 1b, c and Table S1). We further confirmed that none of these seven candidate lncRNAs showed protein coding potential (Supplementary Fig. 1d).

To investigate whether these candidate lncRNAs regulate TLR7 signaling, we isolated primary peritoneal macrophages from 8-week-old C57BL/6 male mice. We then transfected them with a mixture of small interfering RNAs (siRNAs) and antisense oligonucleotides (ASOs) targeting the seven candidate RNAs, respectively. We found that knockdown of lncRNA Gm25395 significantly decreased mRNA levels of the cytokines *Tnf* and *Il6* in mouse peritoneal macrophages upon R837 (Imiquimod, a TLR7 agonist) stimulation (Fig. 1d and Supplementary Fig. 1e), suggesting that Gm25395 might be involved in the regulation of the TLR7-mediated innate immune response. We also detected decreased *Tnf* and *Ifna* mRNA levels upon Gm25395 knockdown in plasmacytoid dendritic cells (pDCs) (Fig. 1e and Supplementary Fig. 1f), indicating that this lncRNA has a similar function in pDCs, which has an important function in SLE development[16]. We therefore focused on this lncRNA for further study.

Since *Gm25395* is located in the ninth intron of mouse gene Atg16l1, we named it *Lnc-Atg16l1*. Lnc-Atg16l1 is capped with N7-methylguanosine (m7G) (Supplementary Fig. 2a) and poly A tailed (Supplementary Fig. 2b–d). We found that Lnc-Atg16l1 is distributed in both the nucleus and cytosol in RAW264.7 cells (Fig. 1f), and Lnc-Atg16l1 expression levels did not change upon R837 stimulation in RAW264.7 cells (Fig. 1g). An RNA pull-down assay confirmed that Lnc-Atg16l1 bound to TLR7 in TLR7-overexpressing RAW264.7 cells (Fig. 1h).

Lnc-Atg16l1 exhibited a significant sequence similarity up to 87% with the human *SCARNA5* gene (Supplementary Fig. 1g). We found that knockdown of lncRNA SCARNA5 significantly decreased mRNA levels of the cytokines *TNF*, *IL6* and *IL1B* in PMA-differentiated THP1 cells upon R848 (Resiquimod, a TLR7 agonist) stimulation (Supplementary Fig. 1h), suggesting conservative function of Lnc-Atg16l1 and SCARNA5 in TLR7-mediated innate immune response. Together, these data suggest that Lnc-Atg16l1 binds to TLR7 and can regulate TLR7 signaling in innate immunity.

Lnc-Atg16l1 promotes TLR7 signaling and inflammation in immune cells

To further determine the function of Lnc-Atg16l1 in regulating TLR7 signaling, we generated two *Lnc-Atg16l1*-deficient (*Lnc-Atg16l1*$^{-/-}$ #1 and *Lnc-Atg16l1*$^{-/-}$ #2) RAW264.7 cell clones using the CRISPR-Cas9 system (Supplementary Fig. 3a, b). The expression and function of Atg16l1 remained unchanged before and after *Lnc-Atg16l1* knockout in RAW264.7 cells (Supplementary Fig. 3c–e). We found that expression of NF-κB signaling-related genes (*Rnf25*, *Hspa1b*, *Stat3* and *Riok3*) were decreased in *Lnc-Atg16l1*$^{-/-}$ cells upon R837 stimulation compared to wild-type (*Lnc-Atg16l1*$^{+/+}$) cells (Fig. 2a and Supplementary Fig. 3f). Gene Ontology (GO) analysis confirmed that genes associated with TLR7-related signaling pathways, such as MyD88-dependent signal pathway and NF-κB transcription factor activity were down-regulated in *Lnc-Atg16l1*$^{-/-}$ cells upon R837 stimulation compared to that in wild-type (*Lnc-Atg16l1*$^{+/+}$) cells (Fig. 2b). Consistently, both two *Lnc-Atg16l1*-knockedout RAW264.7 cell clones produced less TNF and IL-6 than *Lnc-Atg16l1*$^{+/+}$ RAW264.7 cells upon R837 stimulation (Fig. 2c and Supplementary Fig. 3g), and we performed following-up experiments with *Lnc-Atg16l1*$^{-/-}$ #1 RAW264.7 cell clone (referred to as *Lnc-Atg16l1*$^{-/-}$ cells hereafter). We further found that the phosphorylation levels of MAPK (p-P38) and NF-κB (p-P65) were higher in *Lnc-Atg16l1*$^{+/+}$ cells than *Lnc-Atg16l1*$^{-/-}$ cells after R837 stimulation (Fig. 2d). In contrast, Lnc-Atg16l1-overexpressing cells showed upregulated mRNA expression of *Tnf*, *Il6* and *Il1b* compared with that in control cells (Fig. 2e). Additionally, we generated *Lnc-Atg16l1*-deficient C57/B6 mice using CRISPR−Cas9 editing (Supplementary Fig. 4a, b) and detected the decreased *Tnf*, *Il6* and *Il1b* mRNA level in *Lnc-Atg16l1* knockout B cells, BMDMs and BMDCs (Supplementary Fig. 4c, d). These results show that Lnc-Atg16l1 enhances TLR7 downstream signaling and inflammation in various immune cells upon TLR7 activation.

Lnc-Atg16l1 deficiency delays the development of SLE in the BXSB.Yaa mouse model

BXSB mice bearing the Y chromosome-linked autoimmune acceleration mutation (BXSB.Yaa) is an SLE mouse model carrying a *Tlr7* duplication on the Y chromosome. BXSB.Yaa mice develop severe SLE-like phenotypes, including splenomegaly, glomerulonephritis, and the presence of anti-nuclear autoantibodies in contrast to BXSB.B6 mice without the Yaa chromosome segment[17]. To determine whether Lnc-Atg16l1 is involved in the development of TLR7-linked SLE, we generated *Lnc-Atg16l1*-deficient BXSB.Yaa mice (BXSB.Yaa-*Lnc-Atg16l1*$^{-/-}$ mice) by crossing *Lnc-Atg16l1*-deficient female mice with BXSB.Yaa male mice for at least seven generations In addition, the expression of Lnc-Atg16l1 was increased in BXSB.Yaa-*Lnc-Atg16l1*$^{+/+}$ mice compared to BXSB.B6-*Lnc-Atg16l1*$^{+/+}$ mice (Supplementary Fig. 4e), indicating that Lnc-Atg16l1 might play important regulatory roles in BXSB.Yaa mice.

Indeed, we found that compared to BXSB.Yaa-*Lnc-Atg16l1*$^{+/+}$ mice, BXSB.Yaa-*Lnc-Atg16l1*$^{-/-}$ mice displayed limited splenomegaly and less

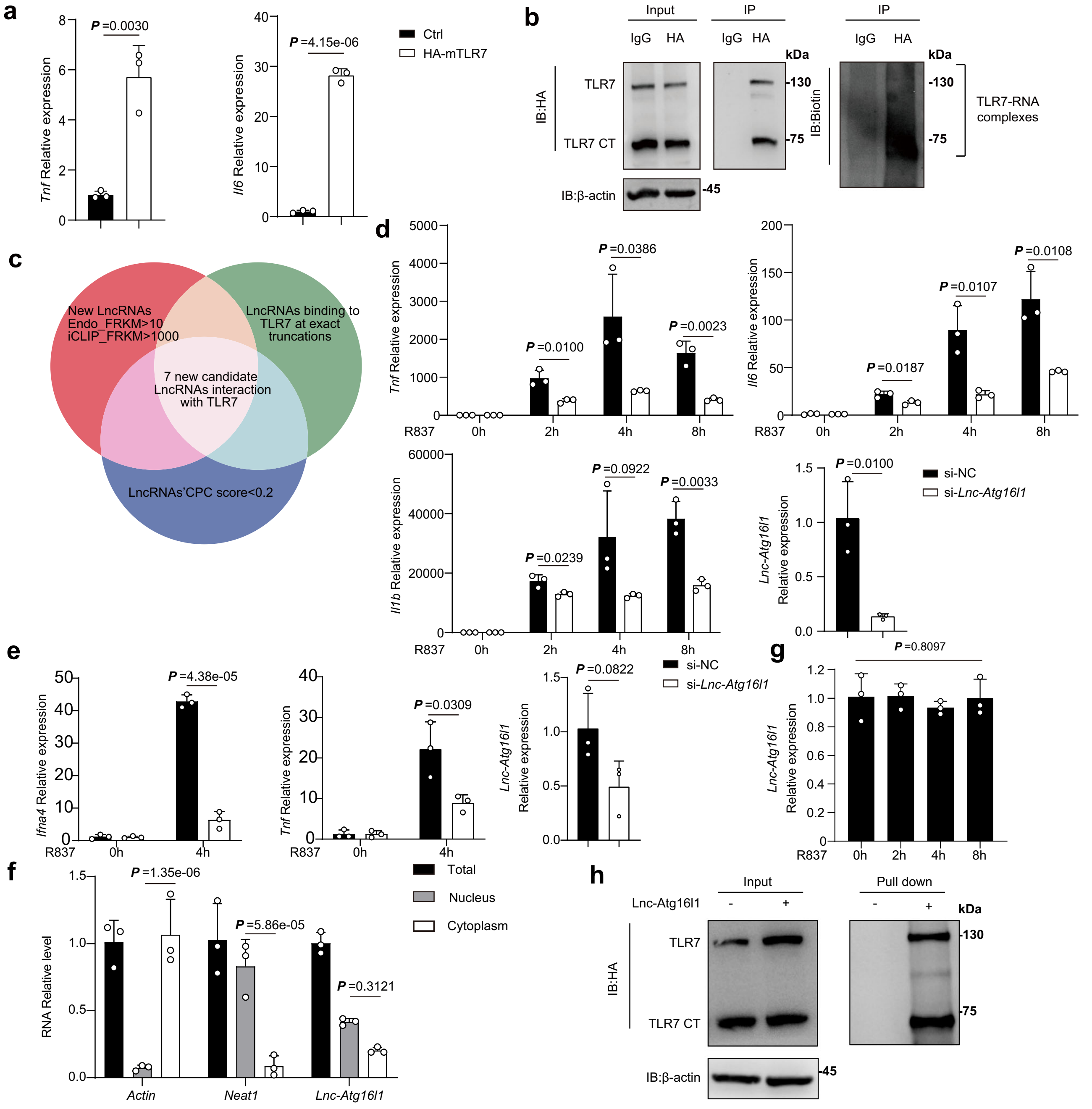

Fig. 1 | Identification of TLR7-binding long noncoding RNA Lnc-Atg16l1. **a** Quantitative RT-PCR (qRT-PCR) analysis of *Tnf* and *Il6* mRNA expression in HA-TLR7-overexpressing and wild-type RAW264.7 cells ($n = 3$). **b** Immunoblot analysis of HA-TLR7 and biotin-labeled RNA-HA-TLR7 complexes in RAW264.7 cells cross-linked with UV at 254 nm. CT, C-terminal fragment. **c** Venn map showing results from iCLIP-seq and Endosome-RNA-seq. **d** qRT-PCR analysis of *Tnf*, *Il6*, *Il1b* and *Lnc-Atg16l1* RNA expressions in peritoneal macrophages transfected with siRNAs and ASOs targeting negative control (NC) or *Lnc-Atg16l1* and stimulated with R837 (5 μg/ml) for indicated hours ($n = 3$). **e** qRT-PCR analysis of *Ifna4*, *Tnf* and *Lnc-Atg16l1* RNA expressions in plasmacytoid dendritic cells transfected with siRNAs and ASOs targeting negative control (NC) or *Lnc-Atg16l1* and stimulated with R837 (5 μg/ml) for 4 h ($n = 3$). **f** qRT-PCR analysis of relative level of *Actin*, *Neat1* and *Lnc-Atg16l1* in nucleus and cytoplasm of RAW264.7 cells ($n = 3$). **g** qRT-PCR analysis of *Lnc-Atg16l1* expression in mouse peritoneal macrophage stimulated with R837 (5 μg/ml) for indicated hours ($n = 3$). **h** Immunoblot analysis of TLR7 pull-down by in vitro transcribed Lnc-Atg16l1 in HA-TLR7-overexpressing RAW264.7 cells. CT, C-terminal fragment. Similar results were obtained from three independent experiments and one representative experiment is shown (**a**, **b**, **d**–**h**). Data in (**a**, **d**–**g**) are shown as mean ± s.d. The *P* values were calculated by a two-tailed unpaired Student's *t* test in (**a**, **d**, **e**). one-way anova test in (**g**) and two-way ANOVA analysis with Sidak's multiple comparisons test in (**f**). Source data are provided as a Source Data file.

severe proliferative glomerulonephritis, as indicated by a reduction of the glomerular PAS-positive deposits (Fig. 3a–d). Serum levels of anti-dsDNA (double-strand DNA) and SmRNP (Smith protein and ribonucleoprotein) antibodies, characteristic of SLE pathogenesis, were also decreased in BXSB.Yaa-*Lnc-Atg16l1*$^{-/-}$ mice (Fig. 3e). Protein levels of TLR7 C-terminal domain and the mRNA expression levels of *Tnf* and *Il1b* in spleens were reduced in BXSB.Yaa-*Lnc-Atg16l1*$^{-/-}$ mice (Fig. 3f, g and Supplementary Fig. 4e). Consistently, the survival of BXSB.Yaa-*Lnc-Atg16l1*$^{-/-}$ mice was significantly prolonged compared to BXSB.Yaa-*Lnc-Atg16l1*$^{+/+}$ mice (Fig. 3h). Overall, these data suggest that Lnc-Atg16l1 promotes SLE-like autoimmune disease development in a TLR7-related mouse model.

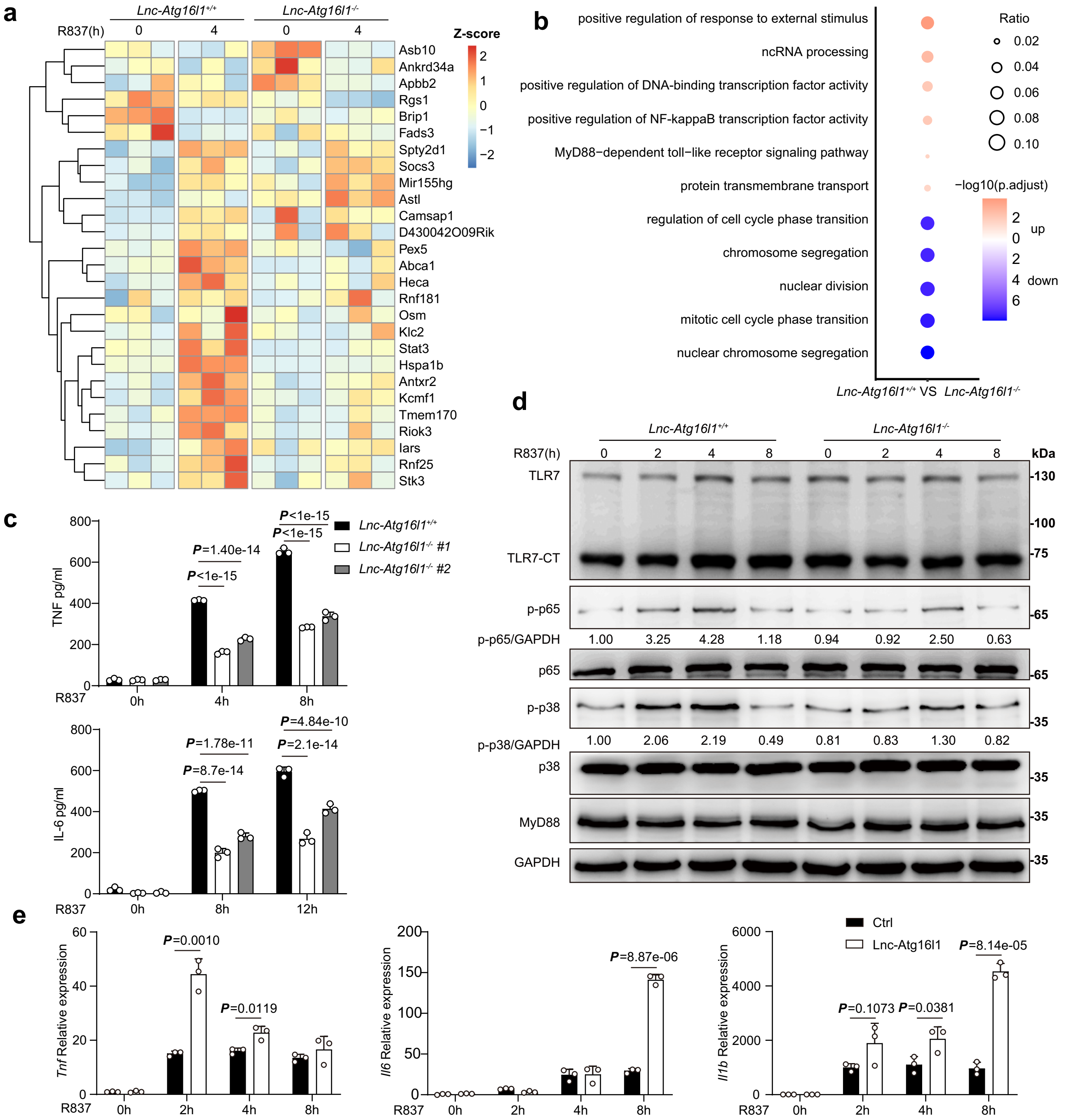

Fig. 2 | Lnc-Atg16l1 enhances TLR7 signaling in macrophages. a Heatmap of differentially expressed genes between *Lnc-Atg16l1*$^{+/+}$ and *Lnc-Atg16l1*$^{-/-}$ RAW264.7 cells with or without stimulation of R837 (5 μg/ml) for 4 h. High expression gene in each group was shown in heatmap with Z-score normalizing of FPKM. **b** Gene Ontology (GO) term analysis of differentially expressed genes between *Lnc-Atg16l1*$^{+/+}$ and *Lnc-Atg16l1*$^{-/-}$ RAW264.7 cells stimulated with R837 (5 μg/ml) for 4 h. **c** ELISA of IL-6 and TNF in the supernatants of *Lnc-Atg16l1*$^{+/+}$, *Lnc-Atg16l1*$^{-/-}$ #1 and *Lnc-Atg16l1*$^{-/-}$ #2 RAW264.7 cells stimulated with R837 (5 μg/ml) for indicated hours ($n = 3$). **d** Immunoblot analysis of TLR7 signaling pathways in *Lnc-Atg16l1*$^{+/+}$, *Lnc-Atg16l1*$^{-/-}$ RAW264.7 cells stimulated with R837 (5 μg/ml) for indicated hours. Quantification of p-p65, p-p38 and GAPDH was applied by ImageJ. (**e**) qRT-PCR analysis of *Tnf*, *Il6* and *Il1b* mRNA expressions in wild-type RAW264.7 cells and *Lnc-Atg16l1*-overexpressing cells stimulated with R837 (5 μg/ml) for indicated hours ($n = 3$). Similar results were obtained from three independent experiments and one representative experiment is shown (**c**–**e**). Data in (**c**, **e**) are shown as mean ± s.d. The *P* values were calculated by a two-tailed unpaired Student's *t* test in (**e**) and two-way ANOVA analysis with Sidak's multiple comparisons test in (**c**). The p.adjust values in (**b**) were calculated by a one-sided hypergeometric distribution with Benjamini-Hochberg (BH) adjusted. Source data are provided as a Source Data file.

Lnc-Atg16l1 promotes TLR7 signaling by binding to both TLR7 and MyD88

Next, we investigated how Lnc-Atg16l1 effectively enhanced TLR7 signaling pathway. TLR7 has two main functional domains: the leucine-rich region (LRR) which binds ligand and the toll-interleukin1-resistance domain (TIR) for MyD88 binding and signal transduction[18]. In order to determine which region of TLR7 binds to Lnc-Atg16l1, we constructed TLR7 truncations (Fig. 4a) and found that Lnc-Atg16l1 bound to both the LRR domain and TIR domain of TLR7 in cells (Fig. 4b). However, an in vitro pull-down assay confirmed that Lnc-

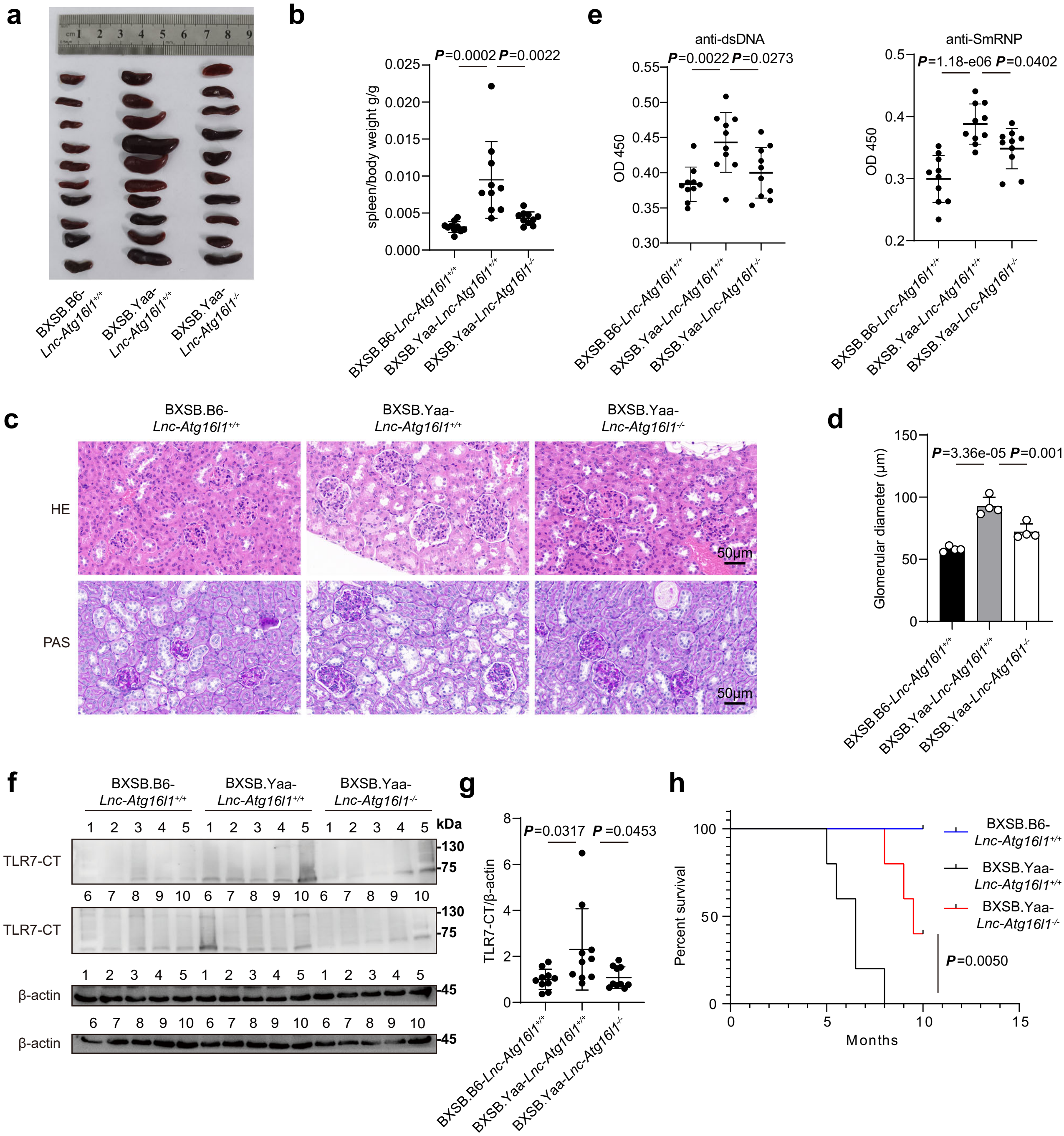

Fig. 3 | Deficiency of *Lnc-Atg16l1* attenuates autoimmune pathogenesis in BXSB.Yaa SLE mouse model. a Pictures showing spleens from BXSB.B6-*Lnc-Atg16l*$^{+/+}$, BXSB.Yaa-*Lnc-Atg16l*$^{+/+}$ and BXSB.Yaa-*Lnc-Atg16l*$^{-/-}$ mice ($n = 10$). **b** Spleen/body weight analysis of BXSB.B6-*Lnc-Atg16l*$^{+/+}$, BXSB.Yaa-*Lnc-Atg16l*$^{+/+}$ and BXSB.Yaa-*Lnc-Atg16l*$^{-/-}$ mice ($n = 10$). **c** Hematoxylin-eosin (H&E) staining and periodic acid/Schiff reagent (PAS) staining of kidney sections from 18-week-old BXSB.B6-*Lnc-Atg16l*$^{+/+}$, BXSB.Yaa-*Lnc-Atg16l*$^{+/+}$ and BXSB.Yaa-*Lnc-Atg16l*$^{-/-}$ mice ($n = 10$). Scale bars, 50 µm. **d** Measurement of the maximum width of renal glomerulus shown in H&E staining slides in Fig.3c. **e** ELISA of serum antibodies to dsDNA and SmRNP from 18-week-old BXSB.B6-*Lnc-Atg16l*$^{+/+}$, BXSB.Yaa-*Lnc-Atg16l*$^{+/+}$ and BXSB.Yaa-*Lnc-Atg16l*$^{-/-}$ mice ($n = 10$). **f**, **g** Immunoblot analysis of TLR7 expression in spleens from 18-week-old BXSB.B6-*Lnc-Atg16l*$^{+/+}$, BXSB.Yaa-*Lnc-Atg16l*$^{+/+}$ and BXSB.Yaa-*Lnc-Atg16l*$^{-/-}$ mice ($n = 10$). Quantification of TLR7 expression by ImageJ. CT, C-terminal fragment (**g**). **h** Survival curves of BXSB.B6-*Lnc-Atg16l*$^{+/+}$, BXSB.Yaa-*Lnc-Atg16l*$^{+/+}$ and BXSB.Yaa-*Lnc-Atg16l*$^{-/-}$ mice ($n = 5$). Similar results were obtained from three independent experiments and one representative experiment is shown (**h**). Data in (**b**, **d**, **e**, **g**) are shown as mean ± s.d. The *P* values were calculated by one-way anova analyses with Tukey's post hoc test in (**b**, **d**, **e**, **g**). and by Log-rank (Mantel-Cox) test in **h**. Source data are provided as a Source Data file.

Atg16l1 directly binds to the TIR domain of TLR7 (Fig. 4c). Since MyD88 also interacts with TIR domain of TLR7[19], we tested and found that Lnc-Atg16l1 can bind MyD88 in vitro (Fig. 4d). Besides, Lnc-Atg16l1 increased interaction between TLR7-TIR and MyD88 in a dose-dependent manner (Fig. 4e). By capturing Lnc-Atg16l1 and its binding proteins with specific probes in cells, we confirmed that Lnc-Atg16l1 bind to TLR7 and MyD88 upon R837 stimulation (Fig. 4f, g). Together, these data suggest that Lnc-Atg16l1 can bind and enhance the interaction between TLR7 and MyD88 to promote downstream signaling.

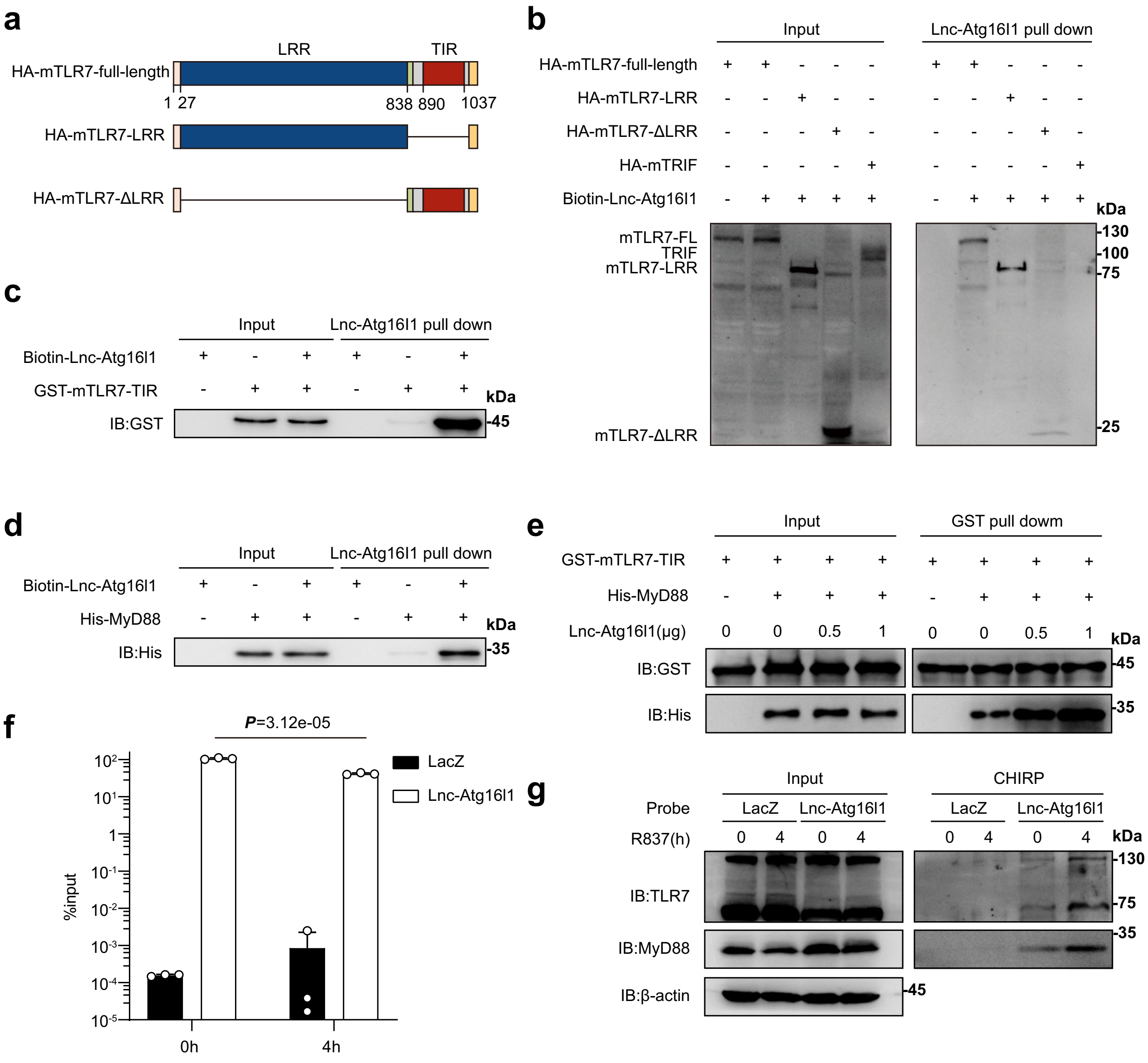

Fig. 4 | Lnc-Atg16l1 promotes TLR7 signaling by strengthening the binding of TLR7 and MyD88. a A schematic diagram of TLR7 domains. **b** Immunoblot analysis of different truncations or full length TLR7 and TRIF pull down by Lnc-Atg16l1 in HEK293T cells. **c**, **d** Immunoblot analysis of TLR7-TIR domain (**c**) or MyD88 (**d**) pull-down by Lnc-Atg16l1. **e** Immunoblot analysis of MyD88 pull-down by TLR7-TIR domain in the presence of increasing Lnc-Atg16l1. **f** qRT-PCR analysis of Lnc-Atg16l1 captured by LacZ (nonspecific) or Lnc-Atg16l1 probes in RAW264.7 cells stimulated with R837 (5 μg/ml) for indicated hours ($n = 3$). **g** Immunoblot analysis of proteins captured by LacZ or Lnc-Atg16l1 probes in RAW264.7 cells stimulated with R837 (5 μg/ml) for indicated hours. Similar results were obtained from three independent experiments and one representative experiment is shown (**b**–**g**). Data in (**f**) are shown as mean ± s.d. The P values were calculated by a two-tailed unpaired Student's t test in (**f**). Source data are provided as a Source Data file.

Lnc-Atg16l1 promotes the downstream effects of TLRs-MyD88 signaling

Considering MyD88 is adaptor for multiple TLRs[5], we wondered whether Lnc-Atg16l1 could also enhance other MyD88-dependent TLRs downstream signaling upon activation. An in vitro pull-down assay indicated that Lnc-Atg16l1 directly bound to the TIR domain of TLR4 and SEFIR domain of TLR9 (Supplementary Fig. 5a). Furthermore, we found that compared to TLR3, the downstream signaling pathways of TLR4 and TLR9 were weakened in *Lnc-Atg16l1* knockout RAW264.7 cells (Supplementary Fig. 5b). The similar results were observed in BMDCs upon LPS or poly (I:C) stimulation (Supplementary Fig. 5c). The above results indicate that Lnc-Atg16l1 could enhance the downstream effects of MyD88-dependent TLRs signaling.

Lnc-Atg16l1 interacts with TLR7 and MyD88 at bases close to U84 and A129

To determine how endogenous Lnc-Atg16l1 binds to both TLR7 and MyD88, we performed iCLIP-seq to define the precise site(s) where Lnc-Atg16l1 interact with TLR7 and MyD88. We found that Lnc-Atg16l1 bound to TLR7 at bases close to U84 and MyD88 at bases near A129, and the interactions between Lnc-Atg16l1 and TLR7/MyD88 increased when TLR7 was activated (Fig. 5a). We designed RNA sequences with repeats of these two binding sites (Fig. 5b). The resulting 84rep RNA fragment specifically bound to TLR7 while the 129rep RNA fragment bound to MyD88 (Fig. 5c, d). We then generated two RNAs containing mutations in the respective binding sites: RNA mut84 and RNA mut129 (Fig. 5b and Table S2). We found that these two mutants could neither

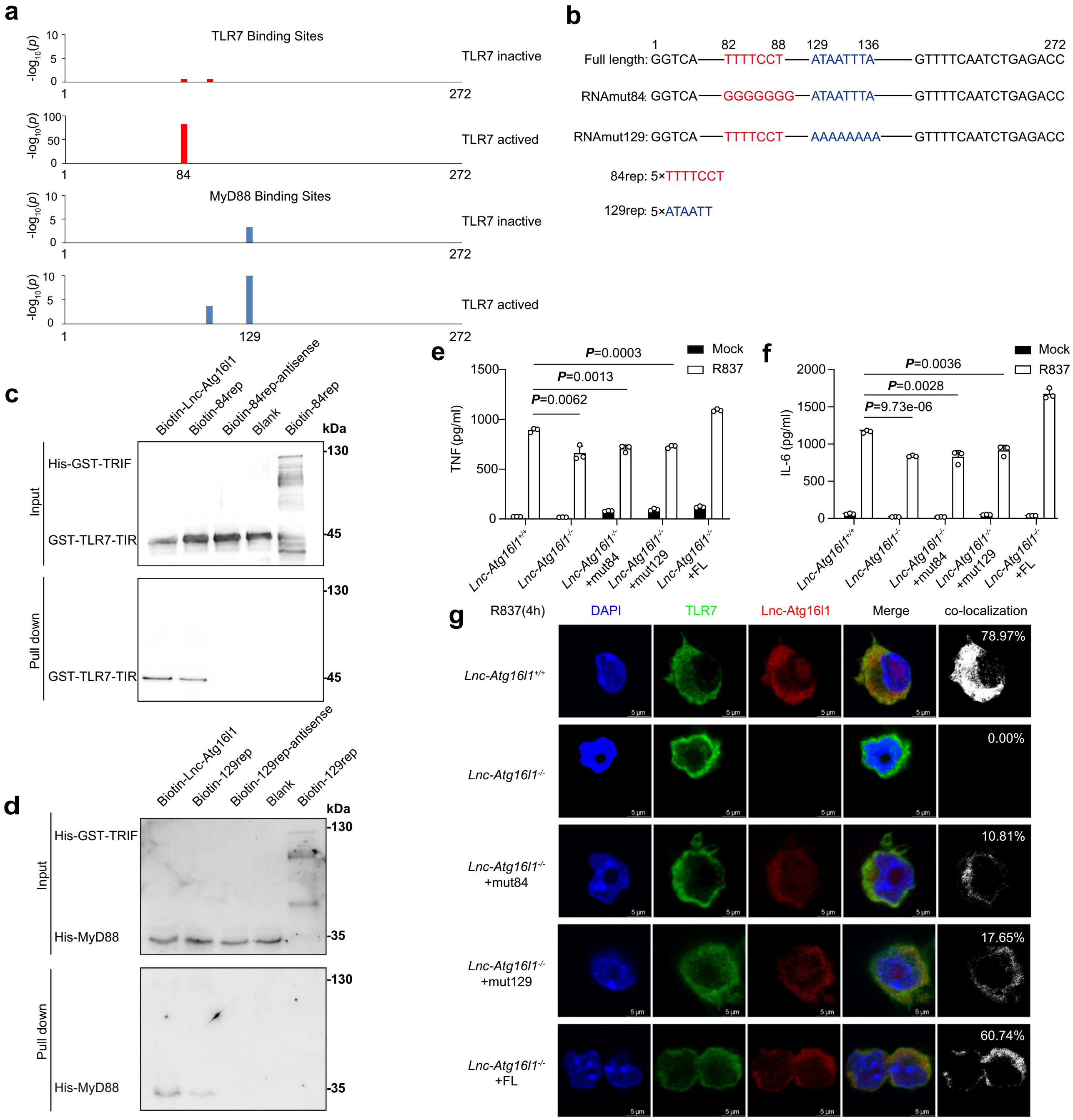

Fig. 5 | Lnc-Atg16l1 interacts with TLR7 and MyD88 at bases close to U84 and A129 respectively to promote innate response in macrophages. a iCLIP truncations analysis of Lnc-Atg16l1 binding sites to TLR7 and MyD88 in RAW264.7 cells before and after TLR7 activation. **b** A schematic diagram of Lnc-Atg16l1 mutations. RNAmut84: sequence mutations around 84th bases. RNAmut129: sequence mutations around 129th bases. **c** Immunoblot analysis of TLR7-TIR domain and His-GST-mTRIF pull-down by Lnc-Atg16l1 or RNAmut84. **d** Immunoblot analysis of MyD88 and His-GST-mTRIF pull-down by Lnc-Atg16l1 or RNAmut129. **e**, **f** ELISA analysis of TNF (**e**) and IL-6 (**f**) in cell culture supernatants of *Lnc-Atg16l1*$^{+/+}$, *Lnc-Atg16l1*$^{-/-}$ and *Lnc-Atg16l1*$^{-/-}$ RAW264.7 cells rescued by RNAmut84, RNAmut129 or Lnc-Atg16l1 and stimulated with R837 (5 μg/ml) for 8 h or 12 h ($n = 3$). **g** Immunofluorescence analysis of co-localization of TLR7 (green) with Lnc-Atg16l1 or mutations (red) in RAW264.7 cells stimulated with R837 (5 μg/ml) for 4 h. Nuclei were stained with DAPI (blue). Scale bars, 5 μm. Similar results were obtained from three independent experiments and one representative experiment is shown (**c**–**g**). Data in (**e**, **f**) are shown as mean ± s.d. The P values were calculated by a two-tailed unpaired Student's t test in (**e**, **f**), and by poisson distribution in (**a**). Source data are provided as a Source Data file.

bind to TLR7/MyD88 (Supplementary Fig. 6a, b) nor rescue the production of TNF and IL-6 in *Lnc-Atg16l1*$^{-/-}$ RAW264.7 cells upon R837 stimulation (Fig. 5e, f and Supplementary Fig. 6c). In addition, Lnc-Atg16l1, but not Lnc-Atg16l1 mutants, co-localized with the TLR7 in the cytoplasm upon R837 stimulation (Fig. 5g). These results suggest that TLR7 binds close to U84 and MyD88 binds near A129 of Lnc-Atg16l1 to activate the TLR7 signaling pathway.

Lnc-Atg16l1 enhances TLR7 signaling through Stem-Loop structure changes

RNA secondary structure plays important roles in diverse biological processes[19]. Because the expression of Lnc-Atg16l1 remained unchanged during R837 stimulation (Fig. 1g), we hypothesized that changes in Lnc-Atg16l1 secondary structure might promote TLR7 signaling. To probe the secondary structure of Lnc-Atg16l1 before and after TLR7

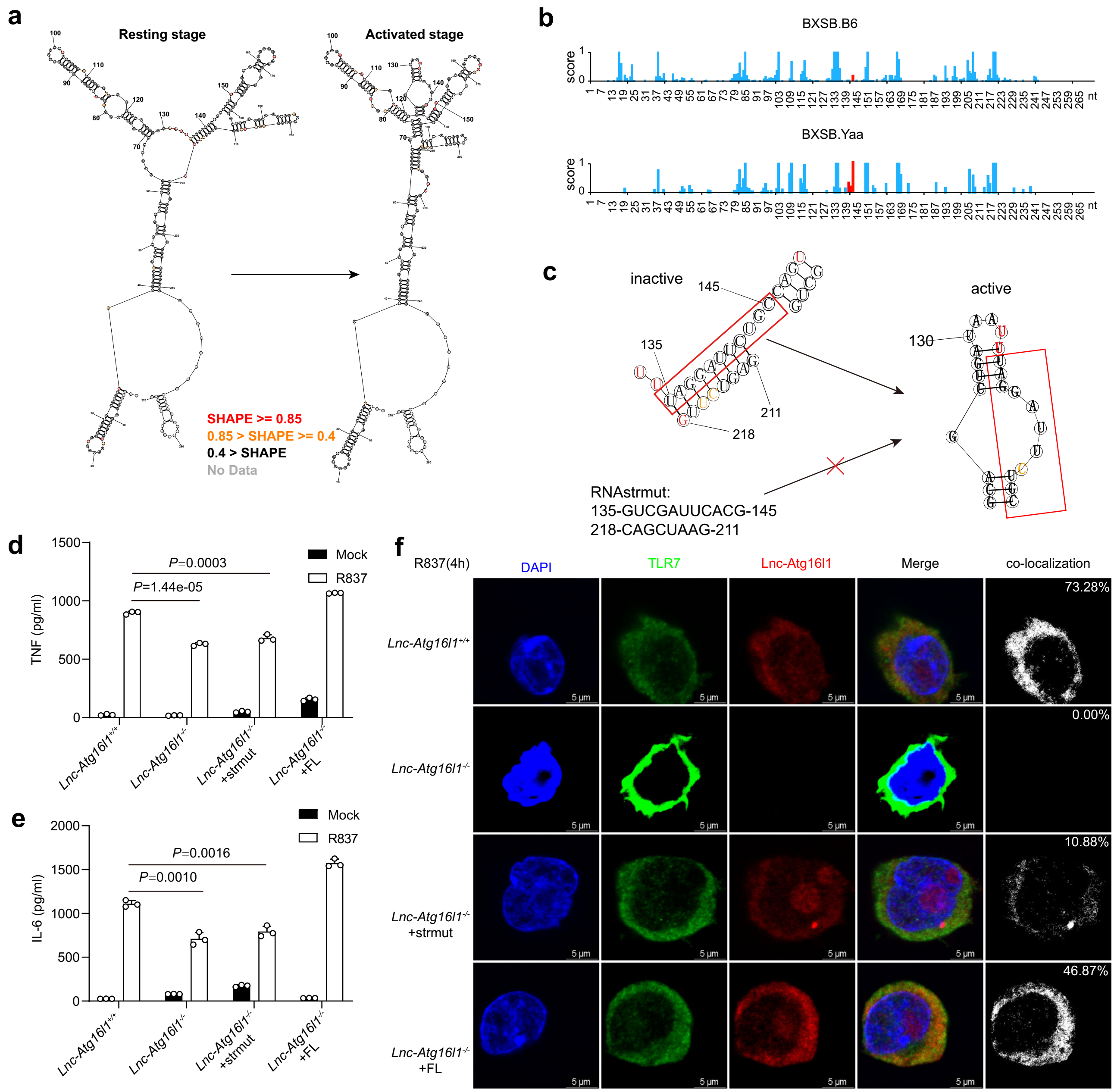

Fig. 6 | Lnc-Atg16l1 enhances TLR7 signaling and innate inflammatory response through its structural changes. a Lnc-Atg16l1 secondary structures calculated by icSHAPE reactivity score before or after TLR7 activation. Color shows icSHAPE reactivity score at each nucleotide. **b** IcSHAPE reactivity score analysis of Lnc-Atg16l1 in spleens from BXSB.Yaa or BXSB.B6 mice. **c** A schematic diagram showing possible structural changes between Lnc-Atg16l1 and RNAstrmut before and after TLR7 activation. **d**, **e** ELISA analysis of TNF (**d**) and IL-6 (**e**) in supernatants of *Lnc-Atg16l1*$^{+/+}$, *Lnc-Atg16l1*$^{-/-}$, and *Lnc-Atg16l1*$^{-/-}$ RAW264.7 cells rescued by RNAstrmut or Lnc-Atg16l1 and stimulated with R837 (5 μg/ml) for 8 or 12 h ($n = 3$). **f** Immunofluorescence analysis of co-localization of TLR7 (green) with Lnc-Atg16l1 or mutations (red) in RAW264.7 cells stimulated with R837 (5 μg/ml) for 4 h. Nuclei were stained with DAPI (blue). Scale bars, 5 μm. Similar results were obtained from three independent experiments and one representative experiment is shown (**d**–**f**). Data in (**d**, **e**) are shown as mean ± s.d. The *P* values were calculated by a two-tailed unpaired Student's *t* test in (**d**, **e**). Source data are provided as a Source Data file.

activation, we performed an in vivo click selective 2-hydroxyl acylation and profiling (icSHAPE)[20] experiment in RAW264.7 cells. We found that the shape of Lnc-Atg16l1 was similar to a clover at resting stage: residues around U84 were located at the top of one stem, while A129 was located at the middle loop between two stems (Fig. 6a). After TLR7 activation, the structure of Lnc-Atg16l1 changed to a four-leaf clover, and the sequences around A129 were located at the top of a new stem (Fig. 6a). This alteration in the Lnc-Atg16l1 structure might reduce steric hindrance, allowing interaction with TLR7 and MyD88. To verify this structural change in vivo, we also performed icSHAPE-seq in spleens from 18-week-old BXSB.Yaa and BXSB.B6 mice, and obtained almost the same structures changes of Lnc-Atg16l1 as that before or after TLR7 activation in RAW264.7 cells (Supplementary Fig. 7a), which might be caused by a prominent structure change at bases 140-142 of Lnc-Atg16l1 with analysis of truncation score. In BXSB.B6 mice, these three bases were largely located within a double stranded structure. However, in BXSB.Yaa mice, these three bases were in a single stranded region (Fig. 6b). These data suggest that a secondary structure change in Lnc-Atg16l1 might be associated with TLR7 activation and linked to SLE development.

To confirm that changes in Lnc-Atg16l1 structure have a functional outcome, we designed RNAstrmut, a mutated Lnc-Atg16l1 with

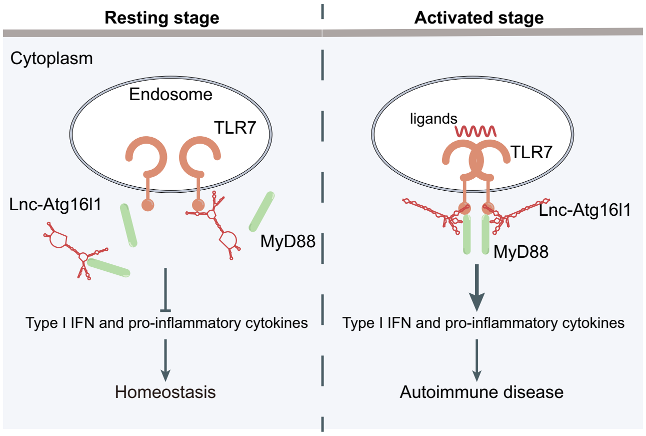

Fig. 7 | Working model for Lnc-Atg16l1 promotion of TLR7 signaling and related autoinflammation through its secondary structure changes. In the resting stage, Lnc-Atg16l1 binds to TLR7 and Myd88 at low levels. After TLR7 activation, the bases close to U84 of Lnc-Atg16l1 binds to TLR7 and bases near A129 binds to Myd88, by which promotes the interaction between TLR7 and Myd88 through the specific stem-loop structure remodeling and consequently enhances TLR7 downstream signaling to trigger autoimmunity.

changes at bases 135-145 and sites that pair with these residues (Fig. 6c and Table S2). These changes are predicted to disrupt the fourth stem which forms after TLR7 activation, but don't change sequences around TLR7/MyD88 binding sites. As expected, RNAstrmut could still directly bind to TLR7/MyD88 (Supplementary Fig. 7b, c), whereas could not increase the production of TNF and IL-6 in *Lnc-Atg16l1*$^{-/-}$ cells as Lnc-Atg16l1 did (Fig. 6d, e and Supplementary Fig. 7d). In addition, Lnc-Atg16l1, but not RNAstrmut, co-localized with TLR7 upon R837 stimulation (Fig. 6f). Together, these results suggest that changes in Lnc-Atg16l1 secondary structure promote TLR7 signaling (Fig. 7).

Discussion

Self RNAs play important roles in the regulation of PRR-mediated innate immune responses. Lnc-Lsm3b can compete with viral RNAs in the binding of RIG-I to terminate type I IFNs production at late stage of innate response[21]. Lnc-zc3h7a interacted with RIG-I and TRIM25 together to strengthen RIG-I downstream signaling pathway[22]. In addition, many cellular dsRNAs in pathophysiological states have been found to induce aberrant immune activation[23]. Identifying these immunostimulatory self RNAs not only provide targets for treating related immune disorders, but could also benefit the development of immunotherapies. As a critical PRR, TLR7 has been reported to bind several kinds of RNAs[24,25], including miRNAs[26,27], siRNAs[28] and snRNA components[29], but it was not clear whether TLR7 could interact with endogenous lncRNAs. In this study, we identified seven candidate lncRNAs that could bind to TLR7. In addition to Lnc-Atg16l1, we found that Lnc-XLOC_011132 could inhibit TLR7 downstream signaling. While Lnc-XLOC_011132 function and the relationship between these two lncRNAs needs to be further investigated, the identification of these TLR7-binding lncRNAs provides potential regulators and targets for TLR7 signaling and TLR7-related autoimmune diseases. Intriguingly, during our work, Darrah team[30] identified the female-specific X-inactive specific transcript (XIST) long noncoding RNA as a uniquely rich source of TLR7 ligands in SLE. The fragment of XIST can active TLR7 in endosome, while Lnc-Atg16l1 predominantly functions in TIR domain of TLR7 to strengthen the binding between TLR7 and MyD88. We also positively support that Lnc-Atg16l1 and other types of RNAs might provide a source of TLR7 ligands in endosome, which need further investigation.

We identify Lnc-Atg16l1 as a positive regulator of MyD88-dependent TLRs, including TLR4, TLR7 and TLR9, and investigate secondary structure changes of Lnc-Atg16l1. Although TLR7-TIR and MyD88 do not contain RNA-binding domains, recent researches reported the proteins lacking characteristic RNA-binding domains, including metabolic enzymes, heat shock proteins, kinases, transcription factors and chromatin-associated proteins, can bind with lncRNAs to regulate their functions, which are considered as the unconventional RBPs[31,32]. We also demonstrate direct interaction between TLR4 TIR or TLR9 SEFIR domain with Lnc-Atg16l1. MyD88 is reported as an adaptor protein of multiples TLRs, such as TLR2, TLR4 and TLR9, while TLR3 activation is TRIF-dependent. TLR4 downstream signaling pathway is activated by recognizing lipopolysaccharide (LPS) with its LRR domain, the same as TLR9 recognizing CpG DNAs[2]. It's neither reported that TLR4 or TLR9 could interact with RNA, nor other domains of MyD88-dependent TLRs could bind to RNA except LRR domain. We add insights in endogenous RNA's regulation to TLRs. However, whether Lnc-Atg16l1 promotes others MyD88-dependent TLRs' activation in the same mechanism as TLR7 needs to be confirmed in the future. Meanwhile, further investigation is required to address why MyD88 can interact with Lnc-Atg16l1 instead of TRIF, the other TLRs' adaptor.

RNA secondary structure is determined by many factors, including RNA sequence changes, RNA modifications, RNA concentrations, RNA-RBP interactions, and so on. Changes in RNA secondary structure under different physiological and pathological conditions could in turn regulate related cellular processes. For example, the disease-associated variant of lnc13 binds hnRNPD less efficiently than its wild-type counterpart, which may cause lnc13 structure changes and contribute to celiac disease[33]. However, flexibility and variability of RNA challenges its structure analysis in vivo. Recently, emerging technologies such as icSHAPE and PARIS[34]. have combined RNA structure calculation with in vivo probes, providing insights into the connection of RNA structure changes and its function. Structural changes in Zika virus RNA were shown to influence infection efficiency through icSHAPE and PARIS[35]. The mechanism of interaction between circRNAs and PKR was solved by SHAPE-Map[36]. On the other hand, more RNA structure predicting software platforms have been developed with higher accuracy than before, such as SHAMAN[37], UFold[38] and trRosettaRNA[39], which would be great helpful to RNA structure analysis. In this study, we analyze the conformational changes of Lnc-Atg16l1 before and after TLR7 activation using icSHAPE technology and demonstrated how this structural change is involved in the function of Lnc-Atg16l1 in promoting TLR7 downstream signaling. These results provide evidence for the important function of RNA secondary structure changes in regulating pathological processes, which should attach more importance in future studies.

SLE is an autoimmune disease that causes long-term suffering. In our study, after knocking out *Lnc-Atg16l1*, TLR7-related BXSB.Yaa SLE model mice exhibit milder symptoms and lived longer, associated with TLR7 activation decrease. Given that TLR7 is responsible for detecting single-stranded RNA viruses, it is also intriguing to elucidate the effects of Lnc-Atg16l on antiviral immune response. We also demonstrated the human homologous gene *SCARNA5* promoting TLR7 activation in PMA-differentiated THP1 cells. We speculated that SCARNA5 might be a potential target for diseases correlated with TLR7 abnormal activation, such as SLE. Meanwhile, we found that Lnc-Atg16l1 could also bind to TLR4 and TLR9 and the functions of Lnc-Atg16l1 in TLR4 and TLR9-related diseases need a further investigation. Taken together, our findings reveal an RNA structure-mediated mechanism for regulating the innate immune response, and provide a potential strategy and target for the intervention in autoimmune diseases such as SLE.

Methods

Ethics statement

All mouse experiments were performed under the supervision of the Institutional Animal Care and Use Committee (IACUC) of the Institute of Laboratory Animal Science of Chinese Academy of Medical Sciences. The experimental design and procedures were reviewed and approved by the animal ethics review board (ACUC-A01-2023-003). All mice were maintained in specific pathogen-free (SPF) conditions, housed in cages with no more than five mice, and kept on in a regular 12 h light/12 h dark cycle (lights on at 7:00 am). The temperature was 24 ± 2 °C and humidity was 40–70%.

Mice and cell lines

C57BL/6 wild-type mice were from Beijing Vital River Laboratory (Beijing, China). BXSB.Yaa mice were from the Jackson Laboratory (Strain #:000740). *Lnc-Atg16l1*-deficient mice were generated using the CRISPR-Cas9 system in a C57BL/6 background. Briefly, two guide RNAs respectively targeting the upstream (5′- GGCTGACTGACTC CTGCTGTGG-3′) and downstream (5′- GGTAAAAGCATCCCATGTG ACGG-3′) regions around *Lnc-Atg16l1* were used to delete this gene. The genotypes of offspring were determined by PCR using the following primers: F: 5′-CTTGCTGTGCCTGGAGTTG-3′; R: 5′-CAAGCTG ACCCTTAAACTCATATTCT-3′. BXSB.Yaa-*Lnc-Atg16l1*$^{-/-}$ mice were generated by crossing *Lnc-Atg16l1*-deficient female mice with BXSB.Yaa male mice for at least seven generations. BXSB.B6 mice crossing with wild type B6 male mice and BXSB.Yaa female mice were used as controls (ctrl). The euthanasia of mice was performed by cervical dislocation under deep anesthesia.

Mouse peritoneal macrophages were isolated from the peritoneal cavities of mice 3 d after injection with thioglycolate medium and were cultured in DMEM medium supplemented with 10% (v/v) FBS.

The HA-mTLR7-overexpressing cell line was generated by transfecting pUNO1-TLR7-HA3X plasmid into RAW264.7 cells followed by 5 μg/ml blasticidin selection. RAW264.7 cells (1101MOU-PUMC000146) and human embryonic kidney cells (HEK293T cells, 3101HUMGNHu17) were from Cell Resource Center, Institute of Basic Medical Sciences, CAMS/PUMC. *Lnc-Atg16l1*-deficient RAW264.7 cells were generated using guide RNAs with the same sequence used in *Lnc-Atg16l1*-deficient mice. Mouse peritoneal macrophages, bone-marrow-derived macrophages and dendritic cells were obtained as previously described[40].

Plasmids and reagents

pUNO1-mTLR7-HA3x (puno1ha-mtlr7) was from Invivogen. HA-mTLR7-LRR, HA-mTLR7-ΔLRR were cloned into pUNO1 plasmids. GST-TLR7-TIR was cloned into pGEX-4t-1 plasmid. pET-28a-His-Myd88 and pSIF-H1 plasmids were kept in our library. pSpCas9(BB)−2A-GFP was from Addgene. spET24-His-GST-3C-TLR4-TIR, spET24-His-GST-3C-TLR9-SEFIR and spET24-His-GST-3C-TRIF plasmids were from SinoBiological.

ELISA kits for mouse IL-6 (M6000B) and TNF (MTA00B) were from R&D Systems. Recombinant Mouse Flt3-Ligand (250-31) and recombinant Mouse IL-4 (214-14) was from Peprotech. Mouse snRNP;Sm Ab ELISA KIT (SU-BN20447) and Mouse ds-DNA Ab ELISA KIT (SU-BN21303) were from Xinquan Technology.

PerCP/Cyanine 5.5 anti-mouse CD19 (115534, 1:100), APC anti-mouse CD11c (117309, 1:100), FITC anti-mouse/human CD45R/B220 (103206, 1:100) and PE-anti mouse CD317 (127010, 1:100) were from BioLegend. Anti-GAPDH (M171-3, 1:2000) and Anti-ACTIN (M177-3,1:2000) were from MBL. Anti-m7G (ab300740) was from abcam. Anti-TLR7 (KT-190, 1:1000 for western blot and 1:200 for immunofluorescence) was customized and purchased from Absea. Anti-IgG (2729S), Anti-Atg16l1 (8089, 1:1000), Anti-P62 (23214, 1:1000), Anti-HA (3724, 1:1000), Anti-p-p65 (3033, 1:1000), Anti-p65 (4764, 1:1000), Anti-p-p38 (4511, 1:1000), and Anti-p38 (8690, 1:1000), Anti-MyD88 (4283, 1:1000), Anti-LC3A/B (12741, 1:500), Anti-GST-HRP (5475, 1:1000) and Anti-His-HRP (12688, 1:1000) were from Cell Signaling Technology.

Flow cytometry and Sorting

Mouse plasmacytoid dendritic cells(pDC) were induced from bone marrow cells in mice and cultured for 7 days in RPMI1640 medium, supplemented with 100 ng/ml recombinant mouse Flt3-L(Peprotech, 250-31). Then, cells were stained with APC-CD11c, FITC-B220 and PE-CD317 for 30 min at 4 °C and washed once with PBS. CD11c$^+$ CD317$^+$ and B220$^+$ pDCs were sorted by flow cytometry on BD FACSAria II for the following experiments. B cell obtained from splenocytes in 8-week-old *Lnc-Atg16l1*$^{+/+}$ and *Lnc-Atg16l1*$^{-/-}$ mice were labeled with PerCP/Cy5.5-CD19. After washed with PBS once, CD19$^+$ B cells were sorted by BD FACSAria II and cultured in RPMI1640 medium, supplemented with 20 ng/ml IL-4(Peprotech, 214-14).

Endosome isolation

HA-mTLR7 stable overexpression cell line was washed using PBS and subjected to crosslinking with 0.3 J/cm^2 UV light in a crosslinker HL-2000 (UVP) at a wavelength of 254 nm. Then endosome isolation was performed with the Minute Endosome Isolation and Cell Fractionation Kit (Invent, ED-028) following the manufacturer's protocol. RNA extracted from the endosome was used for sequencing.

RNA interference

A mixture of siRNA and ASO (20 nmol) was transfected into cells using Lipofectamine RNAiMAX. After transfection for 48 h, cells were stimulated with R837 for indicated hours. Cells were harvested and used for immunoblot or total RNA extraction and qRT-PCR analysis. Sequences targeted by the siRNAs and ASOs are listed in Table S3.

Quantitative RT-PCR

Total RNAs were extracted from pDC, peritoneal macrophage and RAW264.7 cells or mouse organs by RNAfast200 (Fastagen) or TRIzol reagent (Thermo Scientific). Then they were reverse transcribed to cDNA with ReverTra Ace qPCR RT Master Mix (Toyobo). The targets were amplified using SYBR Green Realtime PCR Master Mix (Toyobo). Cycle thresholds (CT) of different samples were normalized to β-actin or to 18S. Primers for qRT-PCR are listed in Table S4.

RNA pull-down assay

Biotin-labeled RNA molecules were generated using an in vitro transcription system including T7 RNA polymerase (Roche), biotin RNA labeling Mix and corresponding buffer (Roche) at 37 °C for 2–3 h. The products were purified using RNeasy Mini Kit (QIAGEN) and DNA templates were digested using RNase-free DNase I (QIAGEN). 1 μg purified RNA was incubated with cell lysates in NT2 buffer containing 500 μg protein purified in vitro or same volume of whole-cell lysates for 1 h at room temperature. Streptavidin M280 beads (Thermo Scientific) were washed then added to the RNA-protein mixed lysates and incubated together for another 2 h at 4 °C. Then beads were washed with NT2 buffer for four times and separated by MagnaRack Magnetic Separation Rack. The complexes of beads-antibodies-proteins were boiled at 100 °C for 10 min in 20 μl loading buffer containing SDS and were prepared for immunoblot analysis.

Individual-nucleotide resolution Cross-Linking and Immunoprecipitation

iCLIP was performed as described previously[41] with the following modifications. In brief, TLR7 inactive and activation RAW264.7 cells were subjected to crosslinking with 0.3 J/cm^2 UV light in a crosslinker HL-2000 (UVP) at the length of 254 nm to capture precise RNA-protein interaction. The cells were then harvested lysed in iCLIP lysis buffer, and clear lysate was immunoprecipitated with anti-HA, anti-TLR7 or anti-MyD88 antibodies (10 μg per 2×10^7 cells) overnight at 4 °C, while IgG was used for IP quality control. Nuclease S1 was used for RNA digestion on-beads (final concentration 1 U/μL or 10 U/μL for 10 min at 30 °C). RNA was dephosphorylated using PNK and linked to the pre-adenylated adapter by T4 RNA Ligase 2, truncated KQ (T4 Rnl2tr R55K, K227Q) (M0373S, NEB). RNA-protein complex was separated on NuPAGE Pre-Cast Bis-TRIS gel and transferred to nitrocellulose (NC) membrane and treated by protease K. Subsequent library construction steps were largely performed as previously described. High-throughput sequencing for relevant experiments was performed by Novogene. The raw data from the iCLIP libraries was analyzed by CLIP tool kit[42] for peak calling and identification of crosslink sites. Raw reads were aligned to mm10 genome assemblies. Peak calling and crosslink-induced truncation sites were calculated and filtered with P value.

Chromatin isolation by RNA purification

Cells with or without R837 stimulation for 4 h were washed three times with PBS. The assay was performed using Magna ChIRP RNA Interactome Kits (Merck Millipore) according to the manufacturer's protocols. Probes used in this assay were as follows: 5′- ACTCTCGGGA ACACACACTG-3′, 5′-GATAGCAGTCAGCTGTGAAC-3′, 5′-TGAGATCAT GCACTGTCACA-3′.

In vivo click selective 2-hydroxyl acylation and profiling experiment (icSHAPE)

IcSHAPE-seq was performed according to published protocol[20] in RAW264.7 cells with or without R837 stimulation for 4 h. The cDNA libraries were sequenced by Novogene (Tianjin, China). Data analysis was also performed according to the published protocol and the icSHAPE reactivity score was calculated. Then icSHAPE reactivity score combined with RNA sequence were used to construct the RNA structure of Lnc-Atg16l1 by RNA structure 6.1 software[43]. The same process was applied to cell samples from spleens of BXSB.Yaa and BXSB.B6 mice after grinding and erythrocyte lysis.

Northern blot analysis of Poly(A)+ RNAs

Poly(A)+ RNAs were enriched by oligo(dT)$_{25}$ Dynabeads (Ambion, cat.no.61005) following the manufacturer's instructions, and treated with 2ul RNase H (AM2293, Invitrogen) in 37 °C for 30 min.10 µg poly(A)+ RNAs were used for electrophoresis in 1% denaturing agarose gel. After that, RNA was transferred to Hybond N+ nylon membrane (RPN119B, Cytiva) and crosslinked by 254 nm ultraviolet light. The cross-linked membrane was hybridized with the NorthernMax kit (AM1940, Invitrogen) according to the manufacturer's protocol. After washing, the membrane was exposed using Chemiluminescent Nucleic Acid Detection Module (89880, Thermo Scientific) following the manufacturer's instructions. Biotin-labeled single-stranded RNA probes were synthesized by in vitro transcription using T7 RNA Polymerase and Biotin RNA Labeling Mix (Roche). The DNA template of RNA probes was amplified according Lnc-Atg16l1 cDNA using the following primers:

Probe1-F: ATTCTGCCAGTGTGTGTTCC;

Probe1-R: TAATACGACTCACTATAGGGTGCATCACAGGTTCTGTT GG;

Probe2-F: ATGTCACAGCCCCTTCCTTG;

Probe2-R: TAATACGACTCACTATAGGGTTCACTCTCGGGAACAC ACAC;

m7G RNA Immunoprecipitation (RIP)

Briefly, total RNA was extracted from 2×10^7 RAW264.7 cells and then incubated with 10 µg anti-m7G (ab300740, abcam) or IgG (2729, CST). The enriched RNA was purified by Direct-zol™ RNA MicroPrep (R2062, Zymo) and evaluated by RT-qPCR.

Immunofluorescence microscopy and fluorescence in situ hybridization assay (FISH)

For RNA FISH assay, RAW264.7 cells were cultured onto glass coverslips in 24-well plates. After being stimulated with R837 for the indicated number of hours, cells were fixed with 4% paraformaldehyde for 10 min, then permeabilized with 0.1% Triton X-100-PBS for 5 min. Cells were incubated with appropriate anti-TLR7 followed by incubation with Alexa Fluor 488-anti-Rat (A11006, Thermo Fisher scientific, 1:500). Then cells were stained with Alexa Fluor 647-conjugated Lnc-Atg16l1 target probes (Sangon Biotech) for 4–16 h at 37 °C and incubated with DAPI. Probes for RNA-FISH were synthetized by Biosearch Technologies (Table S5). The experiments were performed according to the protocol provided by Stellaris RNA FISH (Biosearch Technologies). Fluorescence intensity was detected by Olympus laser-scanning confocal microscope. The co-localization ratio of TLR7 and Lnc-Atg16l1 was calculated by LAS X software.

RNA-seq and Go-ora analysis

Raw data from *Lnc-Atg16l1*$^{+/+}$ and *Lnc-Atg16l1*$^{-/-}$ RAW264.7 cells with or without R837 stimulation were first processed through perl scripts to obtain clean data by removing reads containing adaptor, ploy-N and with low quality. Reference genome and gene model annotation files were directly downloaded from the genome website browser Ensemble. Paired-end clean reads were aligned to the reference genome using HISAT2 2.0.4. The quantification and differential expression analysis were performed by cufflinks series software[44]. Go ora analysis was applied to differential expression genes using R package clusterProfiler (v 4.4.4)[45] with recommended settings. The p-value was calculated by enrichgo function using a one-sided hypergeometric distribution, and the Benjamini-Hochberg (BH) procedure was applied in order to calculate the P-Value Adjusted.

Statistical analysis

Statistical analysis was performed using the GraphPad Prism 8.0. For comparisons, two-tailed Student's t-test, one-way ANOVA analysis with Tukey's post hoc test and two-way ANOVA analysis with Sidak's multiple comparisons test were performed. Survival curve data for mice were analyzed with Log-rank (Mantel–Cox) test and are shown as Kaplan–Meier curves. Data are shown as means ± s.d. $P < 0.05$ was considered as significant.

Reporting summary

Further information on research design is available in the Nature Portfolio Reporting Summary linked to this article.

Data availability

The RNA high throughput sequencing data for RNA-Seq, iCLIP and icSHAPE of this study is deposited in the NCBI GEO dataset under accession code GSE228970. All other study data are included in the article and/or Supplementary Information or from the corresponding author upon request. Source data are provided with this paper.

References

1. Kawai, T. & Akira, S. The role of pattern-recognition receptors in innate immunity: update on Toll-like receptors. *Nat. Immunol.* **11**, 373–384 (2010).
2. Fitzgerald, K. A. & Kagan, J. C. Toll-like receptors and the control of immunity. *Cell* **180**, 1044–1066 (2020).
3. Brown, G. J. et al. TLR7 gain-of-function genetic variation causes human lupus. *Nature* **605**, 349–356 (2022).
4. Elshabrawy, H. A., Essani, A. E., Szekanecz, Z., Fox, D. A. & Shahrara, S. TLRs, future potential therapeutic targets for RA. *Autoimmun. Rev.* **16**, 103–113 (2017).
5. Narayanan, K. B. & Park, H. H. Toll/interleukin-1 receptor (TIR) domain-mediated cellular signaling pathways. *Apoptosis* **20**, 196–209 (2015).
6. Lund, J. M. et al. Recognition of single-stranded RNA viruses by Toll-like receptor 7. *Proc. Natl Acad. Sci. USA* **101**, 5598–5603 (2004).
7. Heil, F. et al. Species-specific recognition of single-stranded RNA via toll-like receptor 7 and 8. *Science* **303**, 1526–1529 (2004).
8. Wang, Y. et al. Decreased expression of the host long-noncoding RNA-GM facilitates viral escape by inhibiting the kinase activity TBK1 via S-glutathionylation. *Immunity* **53**, 1168–1181.e1167 (2020).

9. Liu, W. et al. LncRNA Malat1 inhibition of TDP43 cleavage suppresses IRF3-initiated antiviral innate immunity. *Proc. Natl Acad. Sci. USA* **117**, 23695–23706 (2020).
10. Liu, S. et al. Cis-acting lnc-Cxcl2 restrains neutrophil-mediated lung inflammation by inhibiting epithelial cell CXCL2 expression in virus infection. *Proc. Natl Acad. Sci. USA* **118**, e2108276118 (2021).
11. Liu, J. & Cao, X. RBP-RNA interactions in the control of autoimmunity and autoinflammation. *Cell Res.* **33**, 97–115 (2023).
12. Breaker, R. R. Prospects for riboswitch discovery and analysis. *Mol. Cell* **43**, 867–879 (2011).
13. Keane, S. C. et al. NMR detection of intermolecular interaction sites in the dimeric 5′-leader of the HIV-1 genome. *Proc. Natl Acad. Sci. USA* **113**, 13033–13038 (2016).
14. Ganser, L. R., Kelly, M. L., Herschlag, D. & Al-Hashimi, H. M. The roles of structural dynamics in the cellular functions of RNAs. *Nat. Rev. Mol. Cell Biol.* **20**, 474–489 (2019).
15. Huppertz, I. et al. iCLIP: protein–RNA interactions at nucleotide resolution. *Methods* **65**, 274–287 (2014).
16. Liu, J., Zhang, X. & Cao, X. Dendritic cells in systemic lupus erythematosus: from pathogenesis to therapeutic applications. *J. Autoimmun.* **132**, 102856 (2022).
17. Kono, D. H. & Theofilopoulos, A. N. Genetics of SLE in mice. *Springe. Semin Immunopathol.* **28**, 83–96 (2006).
18. Zhang, Z. et al. Structural analysis reveals that toll-like receptor 7 is a dual receptor for guanosine and single-stranded RNA. *Immunity* **45**, 737–748 (2016).
19. Diebold, S. S., Kaisho, T., Hemmi, H., Akira, S. & Reis e Sousa, C. Innate antiviral responses by means of TLR7-mediated recognition of single-stranded RNA. *Science* **303**, 1529–1531 (2004).
20. Flynn, R. A. et al. Transcriptome-wide interrogation of RNA secondary structure in living cells with icSHAPE. *Nat. Protoc.* **11**, 273–290 (2016).
21. Jiang, M. et al. Self-recognition of an inducible host lncRNA by RIG-I feedback restricts innate immune response. *Cell* **173**, 906–919.e913 (2018).
22. Lin, H. et al. The long noncoding RNA Lnczc3h7a promotes a TRIM25-mediated RIG-I antiviral innate immune response. *Nat. Immunol.* **20**, 812–823 (2019).
23. Chen, Y. G. & Hur, S. Cellular origins of dsRNA, their recognition and consequences. *Nat. Rev. Mol. Cell Biol.* **23**, 286–301 (2022).
24. Jockel, S. et al. The 2′-O-methylation status of a single guanosine controls transfer RNA-mediated Toll-like receptor 7 activation or inhibition. *J. Exp. Med.* **209**, 235–241 (2012).
25. Sarvestani, S. T. et al. Inosine-mediated modulation of RNA sensing by Toll-like receptor 7 (TLR7) and TLR8. *J. Virol.* **88**, 799–810 (2014).
26. Wang, Y. et al. Injured liver-released miRNA-122 elicits acute pulmonary inflammation via activating alveolar macrophage TLR7 signaling pathway. *Proc. Natl Acad. Sci. USA* **116**, 6162–6171 (2019).
27. Zou, L. et al. Brain innate immune response via miRNA-TLR7 sensing in polymicrobial sepsis. *Brain Behav. Immun.* **100**, 10–24 (2022).
28. Bao, M., Yi, Z. & Fu, Y. Activation of TLR7 inhibition of mycobacterium tuberculosis survival by autophagy in RAW 264.7 macrophages. *J. Cell Biochem.* **118**, 4222–4229 (2017).
29. Negishi, H. et al. Identification of U11snRNA as an endogenous agonist of TLR7-mediated immune pathogenesis. *Proc. Natl Acad. Sci. USA* **116**, 23653–23661 (2019).
30. Crawford, J. D. et al. The XIST lncRNA is a sex-specific reservoir of TLR7 ligands in SLE. *JCI insight* **8**, e169344 (2023).
31. Albihlal, W. S. et al. Unconventional RNA-binding proteins: an uncharted zone in RNA biology. *FEBS Lett.* **592**, 2917–2931 (2018).
32. Conrad, T. et al. Serial interactome capture of the human cell nucleus. *Nat. Commun.* **7**, 11212 (2016).
33. Castellanos-Rubio, A. et al. A long noncoding RNA associated with susceptibility to celiac disease. *Science* **352**, 91–95 (2016).
34. Lu, Z. et al. RNA duplex map in living cells reveals higher-order transcriptome structure. *Cell* **165**, 1267–1279 (2016).
35. Li, P. et al. Integrative analysis of Zika Virus Genome RNA structure reveals critical determinants of viral infectivity. *Cell Host Microbe* **24**, 875–886.e875 (2018).
36. Liu, C. X. et al. Structure and degradation of circular RNAs regulate PKR activation in innate immunity. *Cell* **177**, 865–880.e821 (2019).
37. Panei, F. P. et al. Identifying small-molecules binding sites in RNA conformational ensembles with SHAMAN. *Nat. Commun.* **15**, 5725 (2024).
38. Fu, L. et al. UFold: fast and accurate RNA secondary structure prediction with deep learning. *Nucleic Acids Res.* **50**, e14 (2022).
39. Wang, W. et al. trRosettaRNA: automated prediction of RNA 3D structure with transformer network. *Nat. Commun.* **14**, 7266 (2023).
40. Wang, W. et al. RNF122 suppresses antiviral type I interferon production by targeting RIG-I CARDs to mediate RIG-I degradation. *Proc. Natl Acad. Sci. USA* **113**, 9581–9586 (2016).
41. Zarnegar, B. J. et al. irCLIP platform for efficient characterization of protein-RNA interactions. *Nat. Methods* **13**, 489–492 (2016).
42. Shah, A., Qian, Y., Weyn-Vanhentenryck, S. M. & Zhang, C. CLIP Tool Kit (CTK): a flexible and robust pipeline to analyze CLIP sequencing data. *Bioinformatics* **33**, 566–567 (2017).
43. Reuter, J. S. & Mathews, D. H. RNAstructure: software for RNA secondary structure prediction and analysis. *BMC Bioinform.* **11**, 129 (2010).
44. Trapnell, C. et al. Differential gene and transcript expression analysis of RNA-seq experiments with TopHat and Cufflinks. *Nat. Protoc.* **7**, 562–578 (2012).
45. Wu, T. et al. clusterProfiler 4.0: a universal enrichment tool for interpreting omics data. *Innovation* **2**, 100141 (2021).

Acknowledgements

We thank Dr. Jiacheng Wu for critically reading this manuscript. This work was supported by grants from the National Natural Science Foundation of China (82388201 to X.C.) and the CAMS Innovation Fund for Medical Sciences (2021-I2M-1-017 to X.C.).

Author contributions

X.C. supervised the study; Z.Y., S.J., and L.L. performed the experiments; Y.M. generated the knocked-out mice; S.L. and B.W. provided reagents and helpful discussion. Z.Y., S.J., and X.C. analyzed data and wrote the paper.

Competing interests

The authors declare no competing interests.

Additional information

Supplementary information The online version contains supplementary material available at https://doi.org/10.1038/s41467-024-54674-4.

Correspondence and requests for materials should be addressed to Xuetao Cao.

Peer review information *Nature Communications* thanks Vasileios Kyttaris, Osamu Takeuchi and the other, anonymous, reviewer(s) for their contribution to the peer review of this work. A peer review file is available.